MICROSCOPE: the test of the equivalence principle in space and its final data processing

Quentin Baghi, Joel Bergé, Gilles Metris, Manuel Rodrigues, Alain Robert

MICROSCOPE: the test of the equivalence principle in space and its final data processing

Q. BAGHI[1], J. BERGE[2], G. METRIS[3], A. ROBERT[4], M. RODRIGUES[2]
[1] *CEA, Centre de Saclay, IRFU/DPhP, 91191 Gif-sur-Yvette, France*
[2] *DPHY, ONERA, Université Paris Saclay, F-92322 Châtillon, France*
[3] *Université Côte d'Azur, Observatoire de la Côte d'Azur, CNRS, IRD, Géoazur, F-06560 Valbonne, Fr.*
[4] *CNES, Centre Spatial de Toulouse, F-31401 Toulouse, France*

Launched in April 2016, the MICROSCOPE satellite ended its operations in October 2018 with the deployment of its deorbitation wings. MICROSCOPE aims at testing the equivalence principle (EP), the funding hypothesis of general relativity established by Einstein in 1915. In December 2017, first results based on only 7% of the total data improved the best laboratory results by one order of magnitude. The challenging data processing, which has continued since then, has delivered its final results currently under peer review. This presentation focuses on the two topics on which a lot of effort has been put: the impact of glitches and thermal variations on the data. These errors were likely to be in competition with a potential violation signal. We were able to reduce the systematic error by a significant magnitude with respect to the 2017's evaluation thanks to the developed processing and analysis.

1 Introduction

The universality of free-fall (UFF) has been recognized since Galileo rolled objects down inclined planes and found that they all undergo the same acceleration provided that they are in a small enough region of space. In other words, all objects within the same gravitational field fall at the same rate, independently of their mass and composition. Applying Newton's second law to a freely-falling test mass on Earth, one can restate the UFF as the proportionality between the gravitational mass m_G and the inertial mass m_I, with the same proportionality constant for all bodies: this is the usual definition of the weak equivalence principle (WEP).

At the turn of the 20th century, Einstein generalized the WEP, stating that in small enough regions of spacetime, the non-gravitational laws of physics reduce to those of special relativity. In particular, one cannot detect a gravitational field by means of local experiments. This is known as the Einstein equivalence principle (EEP). A subsequent version, the strong equivalence principle, generalizes the EEP to gravitation. That was the starting point to general relativity (GR).

GR describes gravitation as the simple manifestation of spacetime's geometry, while recovering Newton's description of gravitation as a classical inverse-square law (ISL) force in weak gravitational fields and for velocities small compared to the speed of light. It has so far successfully passed all experimental tests [1]. Standing next to GR, the Standard Model (SM) was built from the realization that the microscopic world is intrinsically quantum. Increasingly large particle accelerators and detectors have allowed for the discovery of all particles predicted by the model, up to the Brout-Englert-Higgs boson [2].

Although both GR and SM leave few doubts about their validity in their respective regimes, difficulties have been lurking for decades. Firstly, the question of whether GR and the SM should

and could be unified remains open. Major theoretical endeavors delivered models such as string theory, but still fail to provide a coherent, unified vision of our world. Secondly, unexpected components make up most of the Universe's mass-energy budget: dark matter and dark energy are the largest conundrums of modern fundamental physics.

GR describes the gravitational force as mediated by a single rank-2 tensor field. There are good reasons to couple matter fields to gravity in this way, but there is no good reason to think that the field equation of gravity should not contain other fields. It is then possible to speculate on the existence of other such fields. For instance, scalar fields that mediate a long range force able to affect the Universe's dynamics should also significantly modify gravity in the solar system, in such a way that GR should not have passed any experimental test. Screening mechanisms have been proposed to alleviate this difficulty [3]. In these scenarios, (modified) gravity is environment-dependent, in such a way that gravity is modified at large scales (low density) but is consistent with the current constraints on GR at small scale (high density). These modified gravity models all predict the existence of a new, fifth force, that should be detectable through a violation of the ISL or of the WEP.

The WEP has been tested for four centuries with increased precision [4]. The concept of a test in space emerged in the 1970s [5]. Its motivation is to take advantage of the quiet environment that space can provide and the benefit of much longer test periods.

In 1999, ONERA (Office National d'Etudes et de Recherches Aérospatiales) and OCA (Observatoire de la Côte d'Azur) proposed the MICROSCOPE mission (MICRO-Satellite à Compensation de traînée pour l'Observation du Principe d'Equivalence) to CNES. Selected within the framework of the MYRIADE micro-satellite line, MICROSCOPE operating at room temperature aims to test the WEP with a more modest accuracy than the space cryogenic missions STEP, QuickSTEP, MiniSTEP or GEOSTEP [6].

It was the start of a long path paved with many pitfalls. After a few years of budget freeze, the project entered the core of its development in 2006 and faced technical difficulties: change to field-emission electric indium propulsion in 2006 and finally to cold gas propulsion in 2009, breakage of the 7 μm gold wire connecting the payload test-masses during the qualification in 2011, 1 ns timing anomaly for the payload digital signal processor (DSP) flight model in 2012, coupling in the electrostatic actuation of the payload during satellite integration test in 2015. All these pitfalls were successfully solved by the core CNES/ONERA/OCA team. At the limit of test-ability on ground and at the limit of performance for each subsystem, these difficulties were never encountered before in ONERA's long experience in accelerometry [7], and show how difficult it is to push back the limits of the state of the art in a space experiment.

After the successful launch in 2016 and overcoming of some anomalies which have fortunately been overcome[8], the satellite provided two and a half years of useful data. In 2017, a first analysis based on only 7% of the eventual science data allowed us to verify the WEP at 2×10^{-14} sensitivity level [9]. This result remains the state-of-the-art until MICROSCOPE's final results which were submitted in the beginning of 2022.

2 MICROSCOPE mission overview

2.1 The WEP test experiment principle

The principle of measurement relies on the comparison of the accelerations of two concentric bodies in orbit around the Earth. As shown in Fig. 1, the X-axis is aligned with the test mass cylinders. In an inertial pointing configuration, once per orbit it is pointing in the same direction of the Earth's gravity field vector. In a perfect case, the difference of acceleration is proportional to the Eötvös parameter defined by the relative ratio of difference of gravitational-to-inertial masses m_{gj}/m_{ij} between two materials j:

$$\delta(2,1) = 2\frac{a_2 - a_1}{a_2 + a_1} = 2\frac{m_{g2}/m_{i2} - m_{g1}/m_{i1}}{m_{g2}/m_{i2} + m_{g1}/m_{i1}}, \tag{1}$$

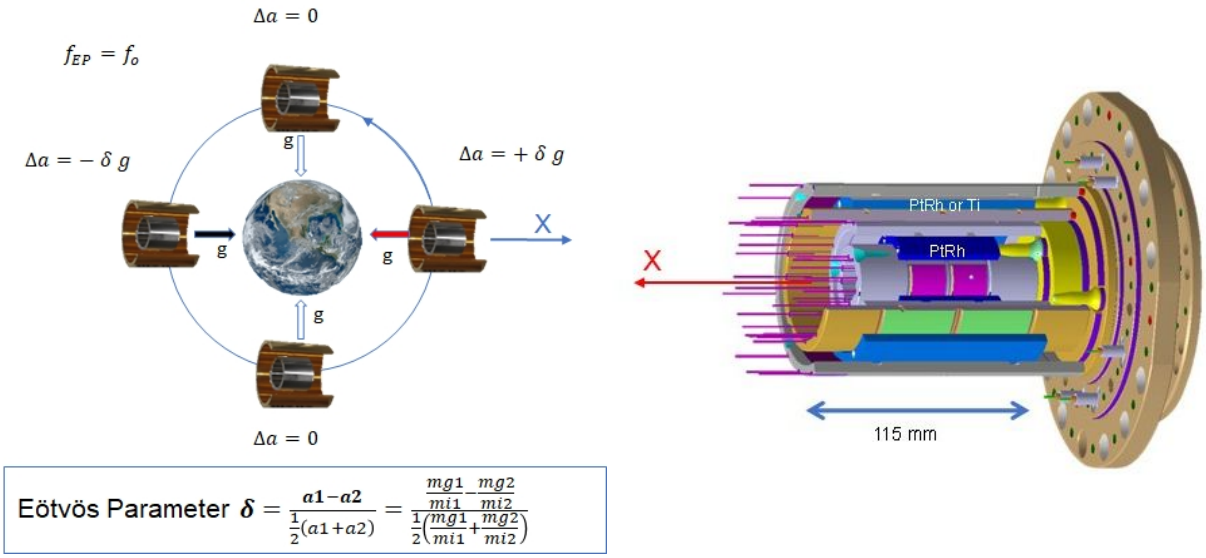

Figure 1 – Schema of experiment principle (left), accelerometer core (right).

where a_j are the acceleration undergone by the two bodies. In this experiment, the test-masses are part of a double concentric accelerometer. The test-masses are finely controlled by electrostatic forces to be motionless with respect to the surrounding electrodes as illustrated in Fig. 1. The forces applied by the set of electrodes are determined by the voltage applied on the test-mass and the one applied on each electrodes as detailed in Ref. [10]. These voltages combined to the geometry characteristics define the applied electrostatic forces and torques to each test-mass which counteract all other effects preventing to keep the test-mass motion-less with respect to the satellite. Thus, if an possible EP violation exists, it could be detected as a signal in the differential acceleration measured by the accelerometer (i.e., the electrostatic force per unit mass) oscillating at the orbital frequency in the case of Fig. 1. The measurement precision can be improved by rotating the satellite about the axis normal to the orbital plane which increases the modulation frequency of the Earth's gravity vector projected onto the X-axis: the EP frequency becomes $f_{\rm EP} = f_{\rm orb} + f_{\rm spin}$, with $f_{\rm orb}$ the orbital frequency and $f_{\rm spin}$ the rotation frequency of the satellite. Two spin frequencies have been used during the mission leading to two test measurement data sets at $f_{\rm EP} \approx 0.9 \times 10^{-3}$ Hz and $f_{\rm EP} \approx 3.1 \times 10^{-3}$ Hz.

2.2 The payload

The payload [10] is composed of two identical differential accelerometers also called sensor units (SUs) except for the test-mass material. Each SU have two concentric hollow cylindrical test-masses surrounded by electrodes engraved on gold-coated silica parts. Each SU is connected to a front-end electronics unit (FEEU) which delivers the voltages to the test-masses and electrodes and transmits the data to the interface control unit (ICU). Each ICU connected to the FEEU contains all the digital electronics and software to operate the test-mass control servo-loops and data conditioning for the satellite and then the ground telemetry. The SU and the FEEU are integrated in a thermal cocoon placed at the core of the satellite which offers a micro-Kelvin stability around the measurement frequencies.

The first SU, called SUREF, comprises two test-masses of the same material : PtRh10 platinum-rhodium alloy containing 90% by mass of Pt ($A = 195.1$, $Z = 78$) and 10% Rh ($A = 102.9$, $Z = 45$). SUREF is dedicated to experiment and accuracy verification (in orbit or on ground within the data processing) as it is supposed to give a null signal at $f_{\rm EP}$. The second SU, called SUEP, comprises two test-masses of different material: the same PtRh10 alloy for the inner test-mass and an aeronautic titanium alloy (TA6V) for the outer test-mass with

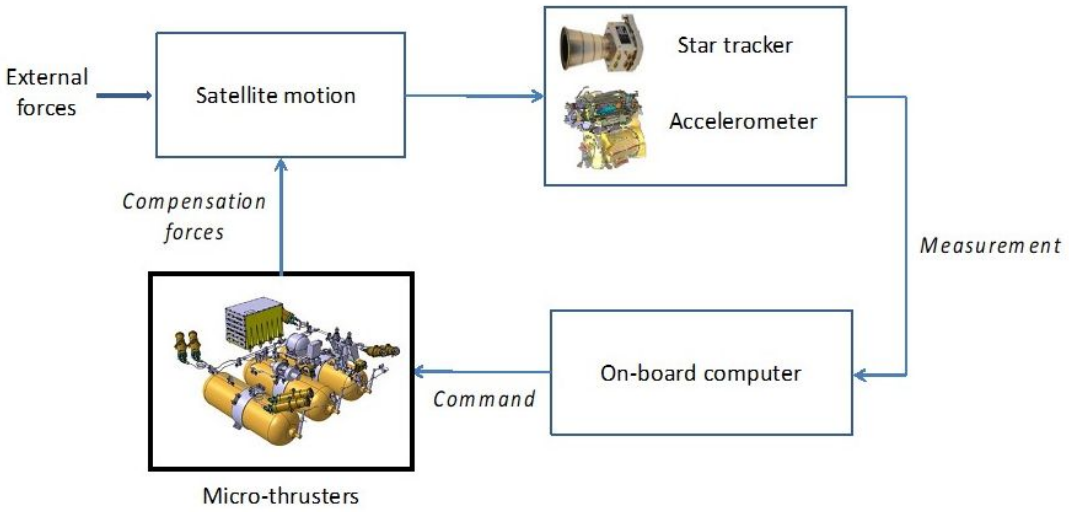

Figure 2 – Satellite Drag-Free and Attitude Control System

the atomic composition 90% of titanium ($A = 47.9$, $Z = 22$), 6% of aluminium ($A = 27.0$, $Z = 13$) and 4% of vanadium ($A = 50.9$, $Z = 23$). SUEP is dedicated to the WEP test.

Each test-mass defines a six-degree-of-freedom accelerometer. In order to operate in the most quiet environment and to get the most accurate orientation of the satellite, the accelerometer outputs are used by the drag-free and attitude control system (DFACS) of the satellite that applies the necessary commands to the cold gas thrusters (Fig. 2). Atmospheric drag, Sun and Earth radiation forces, magnetic torques and all other disturbing sources are compensated in order to nullify the common mode of one of the SU (i.e., either the mean acceleration of the two concentric test-masses or one of the acceleration output). The accelerometer's output or it internal servo loop can be artificially biased at a particular frequency to stimulate the test-mass or the satellite (linear or angular motion) during calibration sessions.

2.3 The drag-free satellite

One of the challenges of the mission objectives is to make the satellite environment as quiet as possible for the payload to prevent any corruption of acceleration measurements.

The MICROSCOPE mission has been developed on the basis of scientific missions exploiting the CNES MYRIADE microsatellite product line whose architecture comprises a platform with generic functional chains (energy, communication, computer, structure, etc.). Some adaptations and modifications were necessary to cope with the unusual performance requirements. Usually, the payloads of the MYRIADE satellites are located on the decoupled upper part of the platform but MICROSCOPE payload module has been uncommonly accommodated at the center of the spacecraft where it can take advantage of a more stable thermal environment (see Figure 3).

The satellite thermal design has been optimised to offer the payload a tight temperature stability: the required stability around the EP test frequency $f_{\rm EP}$ has been set to 1 mK at the sensor unit interface and to 10 mK at the associated analog electronics interface. Active heaters did not operate during the science operations in order to avoid any interference with the payload measurements. Consequently, the thermal control on the satellite purely relied on passive methods: the dissipation of the electronic units was ensured by satellite external radiators. The in-orbit estimated thermal performance exceeded requirements and expectations. The payload was also shielded from the Earth and satellite magnetic field. In addition, the mechanical or electronic micro disturbances were minimized by a careful design and analysis to ensure an optimal environment : choice of multi-layer insulation (MLI) to minimize cracking, minimisation of current loops, study of thermoelastic deformations to estimate internal gravitational effects,

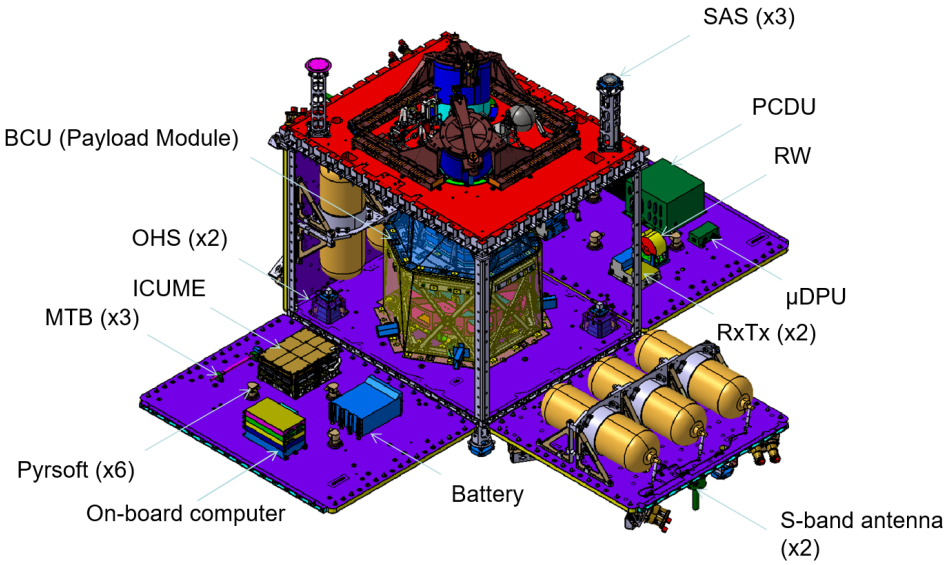

Figure 3 – The cube forming the satellite is open in the picture, the instrument T-SAGE is at the center surrounded by the two 2×3 tanks of the cold gas propulsion system. Once closed the satellite cube measures $1.4\,\mathrm{m}\times1\,\mathrm{m}\times1.5\,\mathrm{m}$ and weighs about 300 kg.

etc.

To counteract non-gravitational forces and torques, an active control of accelerations and attitude of the satellite was implemented through the DFACS (Figure 2). The DFACS used the scientific instrument itself as main sensor for delivering the linear as well as the angular accelerations hybridized with the star tracker measurements. The control laws for acceleration and attitude estimated the total forces and torques to be applied on the satellite which were transformed into 8 micro-thrust commands sent to the cold gas propulsion system placed on two opposite walls of the satellite (Figure 3). The DFACS in-orbit performances allowed to reduce the disturbances by 90 dB around f_{EP} leading to a controlled linear acceleration better than $3\times10^{-13}\,\mathrm{m\,s^{-2}}$, one order of magnitude better than expectation. The satellite attitude was controlled to better than 1 µrad at f_{EP} with an angular velocity stability better than $3\times10^{-10}\,\mathrm{rad\,s^{-1}}$ at f_{EP} in rotating mode, one order of magnitude better than expectation as well. The induced angular acceleration was controlled to better than $10^{-11}\,\mathrm{rad\,s^{-2}}$ at f_{EP}, limiting centrifugal effects due to the off-centring of the test-masses.

Besides, the DFACS was able to receive additional external sine signals at particular frequencies in order to calibrate the instrument (differential scale factor, test-mass alignments and off-centerings, coupling between axes, non-linearity). Particular sessions were also dedicated to thermal sensitivities (see section 3.3) thanks to dedicated heaters.

3 The data processsing

3.1 The measurement equation

A single accelerometer (also called inertial sensor) measures the difference of acceleration between the test-mass of the accelerometer and the center of mass of the satellite. A differential accelerometer yields the difference $\vec{\Gamma}^{(d)} = \vec{\Gamma}^{(1)} - \vec{\Gamma}^{(2)}$ of two such accelerations for two test-masses. The accelerometers are not perfect: they have bias, scale factors departing from unity, non-zero coupling between axes [11]. Moreover, their orientation in the satellite, in space and with respect to the Earth's gravity field, is not perfectly known. That is why the measured

differential acceleration $\vec{\Gamma}^{(d)}$ is not identical to the real one $\vec{\gamma}^{(d)}$, but is related to it as [11]:

$$\vec{\Gamma}^{(d)} = \vec{b_0}^{(d)} + \left[\mathbf{A}^{(c)}\right] \vec{\gamma}^{(d)} + 2 \left[\mathbf{A}^{(d)}\right] \vec{\gamma}^{(c)} + \vec{n}^{(d)}, \tag{2}$$

where

- $\vec{b_0}^{(d)}$ is the difference of bias between the two inertial sensors;
- $\left[\mathbf{A}^{(c)}\right]$ is the common mode sensitivity matrix, close to the identity matrix, which includes scale factors, coupling between axes and global rotation common to the two sensors;
- $\left[\mathbf{A}^{(d)}\right]$ is the differential mode sensitivity matrix, very small, which take into account the difference of characteristics of the two sensors;
- $\vec{\gamma}^{(c)}$ is the common mode acceleration which is mainly due to non-gravitational accelerations acting on the satellite and not on the enclosed test-masses; these non-gravitational accelerations include drag and radiation pressures and the thrust applied to the satellite which is servo-controlled in order to considerably reduce $\vec{\gamma}^{(c)}$ in the frequency band of interest;
- $\vec{n}^{(d)}$ is the (non-white) noise.

In addition, couplings with angular accelerations and non linearities can also arise. These terms are not formally included in the above equation but specific measurement sessions have been dedicated to the identification of such effects and demonstrated that they are negligible [12].

The potential signal of violation of the EP, $\delta(2,1)\vec{g}$, is included in $\vec{\gamma}^{(d)}$ which also contains the gravity gradient and the differential angular acceleration due to the small residual off-centring between the two test-masses [11]:

$$\vec{\gamma}^{(d)} = \delta(2,1)\vec{g}(O_{\rm sat}) + ([\mathrm{T}] - [\mathrm{In}])\vec{\Delta} + \vec{b_1}^{(d)}, \tag{3}$$

where

- $\vec{g}(O_{\rm sat})$ is the gravity acceleration;
- [T] is the gravity gradient tensor;
- [In] is the gradient of inertia matrix;
- $\vec{\Delta}$ is the off-centring vector from the center of test-mass (1) to the center of test-mass (2);
- $\vec{b_1}^{(d)}$ contains the differences between the other small (mainly non gravitational) perturbations acting on the two test-masses.

Only the axis of the cylindrical test-masses, called X, which is much more precise than the other axes is used to estimate the EP signal. Therefore Eq. (2) has to be projected onto the X-axis. This leads to numerous terms (see for example Ref. [11]) but the following considerations lead to simplifications for the reader's convenience:

- the more impacting components of the sensitivity matrix are estimated thanks to dedicated calibrations [12,?];
- the projection of the common mode is corrected thanks to the calibration of $\left[\mathbf{A}^{(d)}\right]$ and the measurement of $\vec{\gamma}^{(c)}$ (which is roughly assimilated to $\vec{\Gamma}^{(c)}$);
- the effect of the angular acceleration (anti-symmetric part of matrix [In]) is neglected (in practice we can correct for it but we have verified that this has no impact at the $f_{\rm EP}$ frequency thanks to the very good stability of the attitude control);

- small terms as the effect of the out-of-orbital-plane component of the off-centring are corrected thanks to dedicated calibrations;
- the tiny impact of the bias at the $f_{\rm EP}$ frequency is included in the evaluation of the systematic effects.

The remaining model used to analyse the measurements along the X-axis writes

$$\Gamma^{(d)}_{x,\rm corr} = \sum_{j=0}^{3} \alpha_j (t-t_0)^j + \delta_x g_x + \delta_z g_z + \Delta'_x S_{xx} + \Delta'_z S_{xz} + n^{(d)}_x. \quad (4)$$

where

- $\delta_x \approx A^{(c)}_{(1,1)} \delta(2,1)$ ($A^{(c)}_{(1,1)}$ being the scale factor along X) is very close to the Eötvös ratio;
- δ_z, a small fraction of $\delta(2,1)$, is in principle too small to be estimated but is included in the model to check the absence of anomaly;
- S_{xx} and S_{xz} are components of the matrix [S] which is the symmetric part of [T] − [In];
- Δ'_x (close to Δ_x) and Δ'_z (close to Δ_z) are "effective" components of the off-centring taking into account the sensitivity matrix;
- $\sum_{j=0}^{3} \alpha_j (t-t_0)^j$ is an empirical polynomial term aiming to absorb the effect of the bias and its slow drift (mainly due to thermal effects).

3.2 Data artefacts

We observed several artefacts in the acceleration measurements collected during the mission. Among them were short instrumental transients, referred to as glitches, rising up to $\sim 10\,\mathrm{nm.s^{-2}}$ and lasting a few seconds in each SU [16]. Due to small differences in the SU's transfer functions, the difference in their acceleration does not result in a perfect cancellation, leaving significant residual signals in the data. While the exact origin of the glitch-generating process is unknown, it is correlated with the satellite's position and orientation with respect to Earth, hinting towards a thermal mechanism related to the illumination by the Earth's albedo with some contribution of the Sun, triggering crackles in the MLI coating of the satellite walls.

Due to this correlation, the distribution of glitch event times was shown to be modulated by the EP frequency. This creates a spurious excess of power in the frequency spectrum, leading to an apparent violation of the EP in some scientific measurement sessions. To prevent this effect from perturbing the test, and in the absence of a proper model accounting for the underlying process, we discarded the data points affected by glitches in the analysis. This operation is called masking, as it amounts to considering corrupted points as missing data. To avoid any noise frequency leakage related to masking, we use a modified expectation-maximization algorithm (M-ECM), an iterative process which estimates the model parameters together with the missing data [17] until a convergence criterion is reached. The estimation of the Eötvös parameter and the reconstructed periodogram we obtain with M-ECM show that the glitch disturbance is successfully mitigated.

Beside glitches, rare jumps in the differential acceleration can be spotted, mostly on SUREF [14]. Note that those jumps are not simple discontinuities, but appear as chaotic, quickly drifting measurements. Fig. 4 shows three such events, two strong ones and one weaker. Although hidden in the noise, those jumps perturb the data analysis and must be discarded. Since this amounts to creating gaps of several hundred seconds, the use of M-ECM is not justified. Rather, we extract "segments" between jumps (or between jumps and any extremity of the session). In the absence of jumps, we call "segment" the entire session. Segments are made as long as possible and

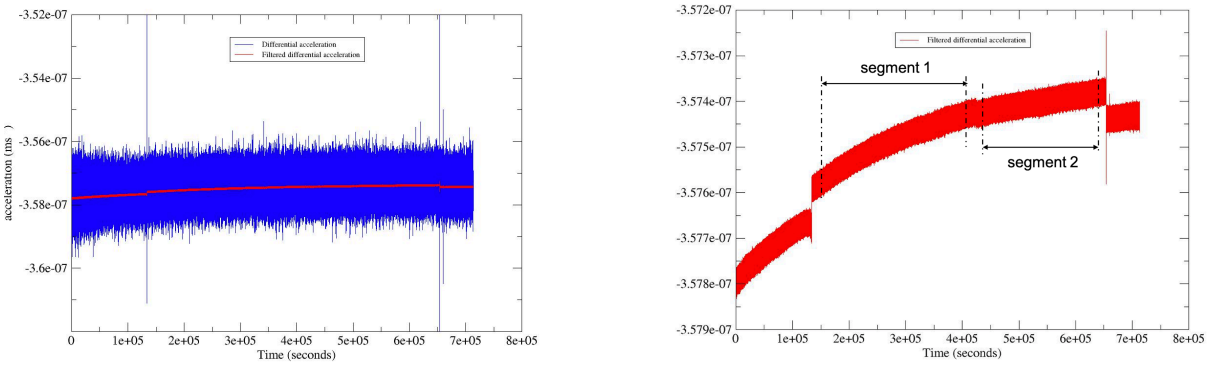

Figure 4 – Example of differential acceleration measured along the x-axis. In this case, discontinuities can be seen (most easily in the filtered data, lower panel), and segments are defined according to them. Each segment is analyzed separately. Figure from Ref. [14].

consist of an even number of orbital periods to ensure that potential contamination by signals at frequencies $mf_{\rm orb} + nf_{\rm spin}$ $(m, n \in \mathbb{N})$ are canceled [14]: this includes the frequency $f_{\rm EP}$. Two of these segments are shown in Fig. 4.

3.3 Main systematic errors: thermal effect

In Ref. [15] the systematic error evaluation was upper-limited by the knowledge of the temperature variations at $f_{\rm EP}$. This estimation was performed on 300 contiguous orbits and showed no temperature signal exceeding from the probe noise. Thus this noise was taken as an upper limit giving a 15 μK temperature variation at $f_{\rm EP}$ at the SU level and hence a systematic acceleration error of $65 \times 10^{-15}\,\mathrm{m\,s^{-2}}$.

Later after the first publication, additional sessions dedicated to temperature sensitivity analysis were performed. In terms of duration, almost 5% of the mission duration was dedicated to thermal characterisation of the satellite and of the payload compared to the 12% of the time dedicated to the EP test with SUEP or 6% of the time dedicated to SUREF. These particular sessions [13] had several objectives: (i) to evaluate the accelerometer thermal sensitivity model; (ii) to confirm that the temperature variations at $f_{\rm EP}$ come from the Earth's albedo entering in the satellite by the FEEU radiator (see Fig. 5); (iii) to better evaluate the temperature variations at $f_{\rm EP}$ during the science sessions. As a first step, to better evaluate the instrument model, the heaters located on the platform at te SU or FEEU level were activated to generate a temperature stimuli and enhance the effect of temperature. Then, calibration sessions were also performed at different temperatures to assess the scale factor dependency on temperature [13]. These experiments led to establish the following model:

$$\begin{aligned}\Gamma^{(d)}_{\rm Tth}(f_{\rm EP}) = &\left[\lambda_{\rm SU}\delta T_{\rm SU}(f_{\rm EP}) + \lambda_{\rm FEEU}\delta T_{\rm FEEU}(f_{\rm EP})\right] \\ &+ \left[\frac{\partial a_{d11}}{\partial T_{\rm SU}}\delta T_{\rm SU}(f_{\rm EP}) + \frac{\partial a_{d11}}{\partial T_{\rm FEEU}}\delta T_{\rm FEEU}(f_{\rm EP})\right]\bar{\Gamma}^{(c)}_{x},\end{aligned} \tag{5}$$

where $\Gamma^{(d)}_{\rm Tth}(f_{\rm EP})$ represents the differential acceleration component of the thermal systematic error at $f_{\rm EP}$, λ_U is the differential acceleration sensitivity to the temperature variations of unit U, a_{d11} the scale factor matching and $\Gamma^{(c)}_x$ the mean common mode acceleration.

The second step confirmed that the SU's temperature variations were correlated to the FEEU's which follows the temperature of the radiator. The purpose of the FEEU radiator is to evacuate the heat dissipation of the electronics to space. A baffle protects the radiator and limits incoming thermal disturbances from Earth's albedo. More than 460 orbits with a particular inclination of the satellite were performed to amplify the impact of Earth's albedo on

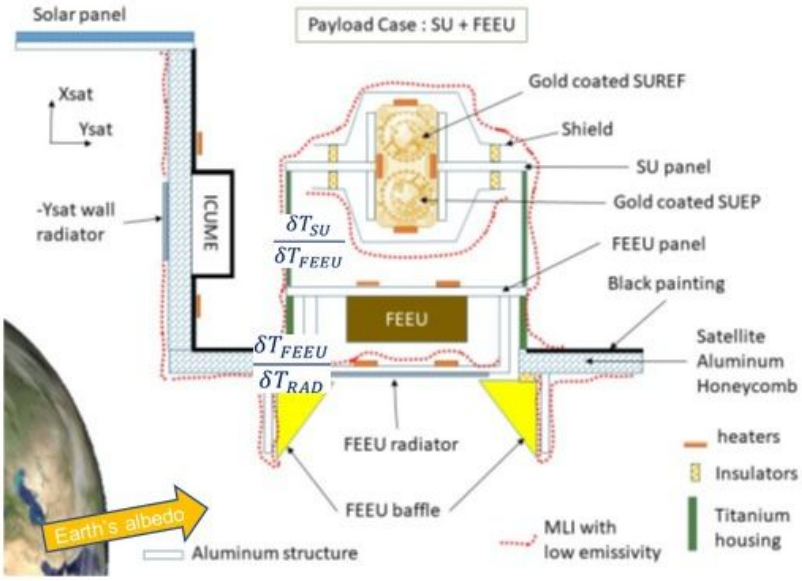

Figure 5 – Payload Case and satellite

the radiator and show that the ratio between FEEU's and SU's temperature variations is higher than 500. Others sessions [13] showed similar behaviour.

As a conclusion of these thermal tests, it was showed that the disturbance process at $f_{\rm EP}$ comes from the radiator and that the SU's temperature in science sessions can be estimated with $\delta T_{\rm SU}(f_{\rm EP}) = \delta T_{\rm FEEU}(f_{\rm EP})/500$. As FEEU's temperature variations come out of the noise in science sessions, it was possible to estimate the SU's temperature for each science session at a level lower than 0.1 μK. By considering this new estimation in Eq. (5), it was possible to estimate the thermal systematics to be lower than $9.3 \times 10^{-15}\,\mathrm{m\,s^{-2}}$, an improvement by a factor of 7.

3.4 The final data process and accuracy

The final results of the MICROSCOPE mission are based on eighteen sessions for SUEP and nine sessions for SUREF, with all data calibrated and systematics fully characterized [14]. A handful of sessions were discarded because of non-linearities at the beginning of the mission, before the control loop's electronics was upgraded. A few others were discarded because of rare anomalies.

Beside EP-test sessions, in-flight calibration sessions are designed to estimate parameters so that the signals sourced by those parameters have a favourable signal-to-noise ratio (each session being dedicated to one or two parameters). We use the fact that parameters are almost independent to simplify and better control the estimation process with an iterative method based on the ADAM (Accelerometric Data Analysis for MICROSCOPE) code to estimate parameters in the frequency domain [18].

In practice, instrumental defects are parameterized by the $\overrightarrow{b}_1^{(d)}$ and $\overrightarrow{\Delta}$ vectors, as well as the $\left[A^{(d)}\right]$ and $\left[A^{(c)}\right]$ matrices in Eq. (4), with only some of their components impacting the projected acceleration [13,11]. The estimation of Δ'_x and Δ'_z uses their couplings with the Earth gravity gradient, whose strong spectral line at $2f_{\rm EP}$ allows for a direct determination in science data based on an accurate Earth gravity model. Dedicated five-orbit sessions were used to measure Δ'_y, where the satellite was oscillated about the z-axis at a frequency $f_{\rm cal}$ to create a measurable signal driven by Δ'_y. The elements of the first row of the $[A^{(d)}]$ matrix a_{d1i} were measured by shaking the satellite at frequency $f_{\rm cal}$ along each axis (x to measure a_{d11}, y for a_{d12} and z for a_{d13}) in order to drive a measurable signal dependent on those parameters. The

a_{d11} sessions also allowed for a measurement of the differential quadratic factor $K_{2d,xx}$ at $2f_{\rm cal}$. Once the above iterative process converges, the Eötvös parameter is estimated on calibrated data following Eq. (4).

4 Conclusion

The MICROSCOPE mission has delivered its final measurement on October 2018. Since then, the science team has put a lot of effort into verifying all the data. Some of them were discarded because they were found to be out of specification due to saturation, out-of-performance range (micrometeorite impacts) and non-linearity measurements. Due to the periodicity of the satellite cracking occurring at the EP frequency yielding a remaining signal in differential mode, an improvement of the data processing was necessary. Glitches in the data were removed and replaced by a maximum-likelihood noise and signal estimation: this process was verified on simulated violation signal inserted in the real data with very satisfactory results. The estimation of systematic errors have been improved with respect the first results obtained in 2017 to a few 10^{-15} in Eötvös parameter units. The final result is to be announced soon and should place it as a reference for the next decade. The data center has been prepared and will be accessible to the scientific community following the announcement at https://cmsm-ds.onera.fr.

Acknowledgments

The authors express their gratitude to all the different services involved in the mission partners and in particular the French space agency CNES in charge of the satellite. This work is based on observations made with the T-SAGE instrument, installed on the CNES-ESA-ONERA-CNRS-OCA-DLR-ZARM MICROSCOPE mission. ONERA authors' work is financially supported by CNES and ONERA fundings. Authors from Observatoire de la Côte d'Azur (OCA) have been supported by OCA, the French National Center for Scientific Research (CNRS), and CNES. ZARM authors' work is supported by the German Space Agency DLR, with funds of the BMWi (FKZ 50 OY 1305 and FKZ 50 LZ 1802) and by the Deutsche Forschungsgemeinschaft DFG (LA 905/12-1). The authors would like to thank the Physikalisch-Technische Bundesanstalt institute in Braunschweig, Germany, for their contribution to the development of the test-masses with funds from CNES and DLR.

References

1. Will, C. M. The Confrontation between General Relativity and Experiment. Living Reviews in Relativity **17**, 4 (2014); Ishak, M. Testing general relativity in cosmology, Living Reviews in Relativity **22**, 1 (2019).
2. Aad, G. et al. Observation of a new particle in the search for the Standard Model Higgs boson with the ATLAS detector at the LHC, Physics Letters B **716**, 1–29 (2012); Chatrchyan, S. et al. Observation of a new boson at a mass of 125 GeV with the CMS experiment at the LHC, Physics Letters B **716**, 30–61 (2012).
3. Joyce, A., Jain, B., Khoury, J., Trodden, M. Beyond the cosmological standard model, Physics Reports **568**, 1–98 (2015).
4. L. Eötvös, D. Pekár, et E. Fekete, Beiträge zum Gesetz der Proportionalität von Trägheit and Gravität, Ann. Phys. **68**, p. 11 (1922); F. W. Bessel, Versuche über die Kraft mit welcher die Erde Körper von verschiedene Beschaffendheit anzieht, Ann. Phys. Chem. (Poggendorf) **25**, p. 401-17 (1832); P. G. Roll, R. Krotkov, et R. H. Dicke, The equivalence of inertial and passive gravitational mass, Annals Phys. **26**, p. 442-517 (1964); V. B. Braginskii et V. I. Panov, Verification of equivalence of inertial and gravitational masses, Zh. Eksp. Teor. Fiz. **61, p. 873-879**, 1971 (;) S. Schlamminger, K.-Y. Choi, T. A.

Wagner, J. H. Gundlach, et E. G. Adelberger, Test of the Equivalence Principle Using a Rotating Torsion Balance, *Phys. Rev. Lett.* **100**, 4 (041101)2008; T. A. Wagner, S. Schlamminger, J. H. Gundlach, et E. G. Adelberger, Torsion-balance tests of the weak equivalence principle, Class. Quant. Grav. **29**, 18, p. 184002 (2012); J. G. Williams, S. G. Turyshev, et D. H. Boggs, Lunar laser ranging tests of the equivalence principle, Classical and Quantum Gravity **29**, 18, p. 184004 (2012); V. Viswanathan, A. Fienga, O. Minazzoli, L. Bernus, J. Laskar, et M. Gastineau, The new lunar ephemeris INPOP17a and its application to fundamental physics, MNRAS **476**, p. 1877-1888 (2018).

5. P. K. Chapman et A. J. Hanson, An Eötvös Experiment in Earth Orbit, R.W. Davies (Ed.), Proc. Conf. on Experimental Tests of Gravitation Theories **JPL TM**, 33-499, p. 228 (1970); Everitt, C. W. F., Damour, T., Nordtvedt, K., Reinhard, R. Historical perspective on testing the Equivalence Principle, Advances in Space Research **32**, 1297–1300 (2003).
6. Bonneville, R. GEOSTEP: A gravitation experiment in Earth-orbiting satellite to test the Equivalence Principle, Advances in Space Research **32**, 1367–1372 (2003); Sumner, T. J. et al. STEP (satellite test of the equivalence principle), Advances in Space Research **39**, 254–258 (2007).
7. P. Touboul, E. Willemenot, B. Foulon, et V. Josselin, Accelerometers for CHAMP, GRACE and GOCE space missions: synergy and evolution, Bollettino di geofisica teorica ed applicata **40**, 3-4, p. 321-327 (Dec. 1999).
8. M. Rodrigues et al., MICROSCOPE Mission scenario, ground segment and data processing, Class. Quant. Grav., DOI: http://iopscience.iop.org/article/10.1088/1361-6382/ac4b9a.
9. Touboul, P. et al 2019. Space test of the equivalence principle: first results of the MICROSCOPE mission, Classical and Quantum Gravity **36**, 22 (2019).
10. M. Rodrigues et al., MICROSCOPE instrument description and validation, Classical and Quantum Gravity, http://iopscience.iop.org/article/10.1088/1361-6382/ac1619, 2021.
11. Touboul P, Rodrigues M, Métris G, Chhun R, Robert A, Baghi Q, Hardy E, Bergé J, Boulanger D, Christophe B, Cipolla V, Foulon B, Guidotti P Y, Huynh P A, Lebat V, Liorzou F, Pouilloux B, Prieur P and Reynaud S 2020 *arXiv e-prints* arXiv:2012.06472.
12. Chhun R and Microscope team, *Class. Quant. Grav.*, 2021.
13. M. Rodrigues et al., MICROSCOPE: systematic errors, Classical and Quantum Gravity , (2002) http://iopscience.iop.org/article/10.1088/1361-6382/ac49f6.
14. P. Touboul et al., MICROSCOPE Weak Equivalence Principle test and result, submitted to *Class. Quant. Grav.*, 2022.
15. P. Touboul et al., MICROSCOPE Mission: First Results of a Space Test of the Equivalence Principle, *Phys. Rev.* D **119**, 23, p. 231101 (dec. 2017), doi: 10.1103/PhysRevLett.119.231101.
16. J. Bergé, Q.Baghi, A. Robert, M. Rodrigues, B. Foulon, E. Hardy, G. Métris, S. Pires, P. Touboul, MICROSCOPE mission: Statistics and impact of glitches on the test of the weak equivalence principle, *arXiv e-prints*, arXiv:2012.06485, 2020.
17. Q. Baghi, G. Métris, J. Bergé, B. Christophe, P. Touboul, M. Rodrigues, Gaussian regression and power spectral density estimation with missing data: The MICROSCOPE space mission as a case study, *Phys. Rev.* D **93**, 12, p. 122-007 (2016), doi 10.1103/PhysRevD.93.122007.
18. J. Bergé et al., 2022, MICROSCOPE mission: Data analysis principle, Class. Quant. Grav. in press.